

Co-design Optimization of Moving Parts for Compliance and Collision Avoidance

Amir M. Mirzendehtel^a, Morad Behandish^a

^a*Palo Alto Research Center, 3333 Coyote Hill Road, Palo Alto, 94304, CA, USA*

Abstract

Design requirements for moving parts in mechanical assemblies are typically specified in terms of interactions with other parts. Some are purely kinematic (e.g., pairwise collision avoidance) while others depend on physics and material properties (e.g., deformation under loads). Kinematic design methods and physics-based shape/topology optimization (SO/TO) deal separately with these requirements. They rarely talk to each other as the former uses set algebra and group theory while the latter requires discretizing and solving differential equations. Hence, optimizing a moving part based on physics typically relies on either neglecting or pruning kinematic constraints in advance, e.g., by restricting the design domain to a collision-free space using an unsweep operation. In this paper, we show that TO can be used to co-design two or more parts in relative motion to simultaneously satisfy physics-based criteria and collision avoidance. We restrict our attention to maximizing linear-elastic stiffness while penalizing collision measures aggregated in time. We couple the TO loops for two parts in relative motion so that the evolution of each part's shape is accounted for when penalizing collision for the other part. The collision measures are computed by a correlation functional that can be discretized by left- and right-multiplying the shape design variables by a pre-computed matrix that depends solely on the motion. This decoupling is key to making the computations scalable for TO iterations. We demonstrate the effectiveness of the approach with 2D and 3D examples.

Keywords: Co-design, Topology Optimization, Kinematic Design, Collision Avoidance, Collision Measure

1. Introduction

Design for Assembly (DFA) describes a set of principles and guidelines widely used in modern product design that enable manufacturers to improve product quality and performance while reducing assembly time and cost. The DFA process typically begins with a thorough analysis of the product design to identify any potential assembly problems or areas for improvement. Subsequently, through part consolidation and reducing the need for specialized tools and equipment during assembly, the entire design-to-fabrication-to-assembly workflow becomes more sustainable and profitable. Current processes mainly rely on expensive, time-consuming, and labor-intensive iterations. Recent advances in shape and topology optimization (TO) have enabled engineers to explore the feasible design spaces more rapidly and avoid tedious trial and error at the early stages of design.

In recent years, incorporating various physics objectives [1] and manufacturing constraints [2, 3] in TO have been widely researched and significant effort has been spent on developing and refining algorithms for finding high-performance lightweight structures in aerospace [4], automotive [5], and medical [6] applications. However, despite its importance in many engineering design problems, less attention has been paid to incorporating kinematic constraints into the optimization process. One such constraint is collision avoidance, whose incorporation into TO re-

quires simultaneous reasoning about interactions and mechanics of multiple moving parts.

In this study, we develop a TO method to co-design multiple parts in relative motion by coupling stiffness with collision avoidance. TO is a computational design approach to distribute material in 2D or 3D space. Incorporating the collision avoidance constraint into gradient-descent TO requires formulating a collision measure, whose differentiation leads to a locally evaluable sensitivity field with respect to material placement at different locations in the design domain. A challenge is that alterations made to one component could introduce or eliminate collisions with other components. As a result, a co-design process is required in which the components are modified simultaneously, where the evolution of one component directly impacts the design of the rest of the assembly. Further, evaluating pairwise collisions during the entire motion at every optimization loop becomes time intensive.

To the best of our knowledge, there is no co-design method that enables the creation of intricate shapes while accounting for collision under arbitrary movements. This study presents a framework to design sets of components by simultaneously considering collision avoidance along with other constraints such as performance and manufacturing. We focus on mechanics under linear-elastic small deformations and use stiffness as the objective function for physics-based requirements. To ensure collision avoidance, we penalize the objective sensitivity field with the gradi-

ent of collision measures aggregated over time. Specifically, the paper outlines a Pareto-tracing TO method for combining the topological sensitivity field (TSF) [7] with collision gradient [8, 9]. Moreover, to make the collision evaluation scalable for TO iterations, the collision measures are computed using a correlation functional that can be discretized by left- and right- multiplication of the topology-dependent design variables with a pre-computed matrix dependent only on the motion. While other constraints are not the focus of this paper, a general approach for incorporating them with collision constraints using the principles outlined in [10] is demonstrated.

1.1. Related work

Apart from different performance and manufacturing requirements imposed on individual parts, there are other crucial design factors whose consideration requires spatial reasoning about the relative movement (both translation and rotation) of parts. Collision avoidance, in particular, is critical in assembly, packaging, navigation, and accessibility requirements. These factors cannot be simply resolved through techniques commonly utilized in TO, such as design rules or sensitivity filtering. Instead, they are often expressed through kinematic constraints, expressed in a set- and group-theoretic language (such as affine transformations, Boolean operations, and containment relations), in contrast to the language of real-valued functions utilized for (in)equality constraints in TO.

İlieş and Shapiro [11, 12] introduced the unsweep as a fundamental operation in solid modeling, which is used to generate the maximal allowable shape of a rigid part that can move against another part with a given shape while satisfying collision avoidance or containment constraints. The idea of shaping through motion was further generalized to configuration space operations [13] using group morphology [14], which were subsequently used in solving problems in manufacturing analysis and process planning for additive and subtractive processes [15–17].

Maximal sets (including unsweeps) can be represented implicitly (via point membership classification) in terms of pointwise constraints. Noting that every subset of the maximal collision-free set satisfies collision avoidance, unsweep can be used prior to TO to prune the feasible design domain [10]. For applications in which maximal sets cannot be defined, such as accessibility for multi-axis machining, the kinematics constraints can be directly incorporated in the optimization loop through a spatially varying field (e.g., inaccessibility measure field) that augments the primary sensitivity field [2, 18, 19].

Stöckli and Shea [8] proposed a rule-based TO approach for generating collision-free rigid bodies with given inertia properties. They introduced the concept of collision matrix, which needs to be computed only once. The subsequent collision evaluation at each optimization iteration can be achieved through efficient matrix-vector multiplications. This idea was employed in [9] to extend the notion

of maximality to pairs of objects and to incrementally co-generate “maximal pairs” of collision-free parts only based on kinematic constraints.

Current methods for creating shapes that comply with constraints that have to do with collisions and contacts under arbitrary motion are overly restrictive, limiting the potential for more efficient and cost-effective assembly designs. Our method builds on the previous works in [8, 9] to provide a general gradient-based formulation for automated co-design of high-performance collision-free solids.

1.2. Contributions & Outline

This article presents a TO-based computational framework for co-generating collision-free shapes in arbitrary relative motion. We show that:

1. The scope of TO can be broadened to co-optimize moving components of an assembly with respect to physics-based performance and collision avoidance.
2. The collision of *multiple* solids in relative motion can be measured locally and globally to use as a topologically differentiable collision measure for gradient-based optimization.
3. The collision measure can be augmented with other sensitivity fields to attractively and incrementally co-generate sets of collision-free solids.
4. The optimization process can co-generate nontrivial shapes in 2D and 3D.

One possible use-case for this approach is the design of spatial linkages in which the motion is pre-determined from the kinematic analysis. Current approaches typically use simple geometry (e.g., use straight rods for links) to make collision avoidance tractable. Our approach enables designing links of arbitrarily complex shapes to achieve the best mechanical performance while avoiding collisions.

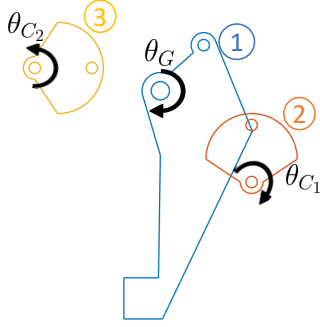
2. Collision Measures

In this section, we briefly review the set-theoretic and discretized formulations for collision measures under motion and provide generalized expressions for multiple parts.

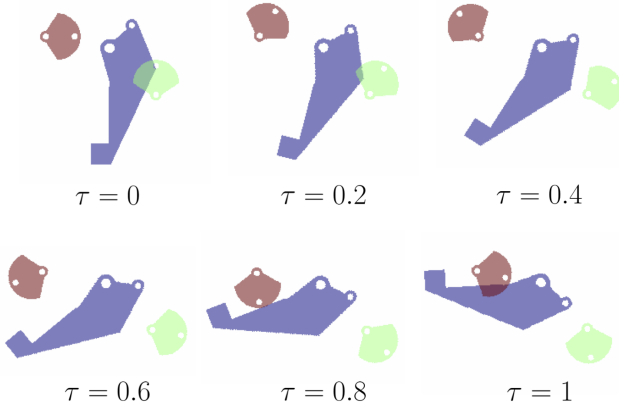
2.1. Set-Theoretic Formulation

Let us consider multiple design domains under motion $\Omega_i \subseteq \mathbb{R}^d$, $i = 1, \dots, N$ for the N solids we aim to co-design ($d = 2, 3$). Let us begin from the given initial designs $S_i \subseteq \Omega_i$ representing the shape of each solid at before applying any motion. Let $M_i \in \text{SE}(d)$ be the motion of the i^{th} solid with respect to a common frame of reference. For instance for one-parametric motions:

$$M_i \triangleq \{\tau_i(t) \mid 0 \leq \tau \leq 1\}, \quad i = 1, \dots, N \quad (1)$$



(a) Motion of the gripper and two cams.



(b) Sample snapshots.

Figure 1: Motion of the Gripper and two cams.

where $\tau_i : [0, 1] \rightarrow \text{SE}(d)$ are continuously time-variant configurations, and can be represented by homogeneous matrices. The displaced solids at any given time $t \in [0, 1]$ are:

$$S_i(t) \triangleq \tau_i(t)S_i = \{\tau_i(t)\mathbf{x} \mid \mathbf{x} \in S_i\}, \quad i = 1, \dots, N \quad (2)$$

Without loss of generality, we assume $\tau_i(0)$ to be identity, so $S_i(0) = S_i, \forall i$, as intended.

To formulate collision measures, it is more convenient to represent the pointsets implicitly via binary membership tests, also called indicator or characteristic functions $\mathbf{1}_{S_i} : \mathbb{R}^d \rightarrow \{0, 1\}$, defined generally by:

$$\mathbf{1}_S(\mathbf{x}) \triangleq \begin{cases} 1 & \text{if } \mathbf{x} \in S, \\ 0 & \text{otherwise.} \end{cases} \quad (3)$$

Note that indicator functions are contra-variant with rigid transformations, i.e., $\mathbf{1}_{\tau S}(\mathbf{x}) = \mathbf{1}_S(\tau^{-1}\mathbf{x})$, meaning that a membership query for a given point against the displaced solid can be computed by displacing the query point along the inverse trajectory and testing its membership against the stationary solid.

Let $M_{i,j} = M_i^{-1}M_j$ stand for the relative motion of S_j as observed from a frame of reference attached to S_i , noting that by kinematic inversion, $M_{j,i} \triangleq M_{i,j}^{-1} = M_j^{-1}M_i$ would represent the relative motion of S_i as observed from

a frame of reference attached to S_j .

$$M_{i,j} \triangleq M_i^{-1}M_j = \{\tau_{i,j}(t) \mid 0 \leq t \leq 1\}, \quad \forall i \neq j \quad (4)$$

where $\tau_{i,j}(t) = \tau_i^{-1}(t)\tau_j(t)$. The displaced solids at any given time $t \in [0, 1]$ in the relative frames are:

$$S_{i,j}(t) \triangleq \tau_{j,i}(t)S_i = \{\tau_{j,i}(t)\mathbf{x} \mid \mathbf{x} \in S_i\}, \quad \forall i \neq j \quad (5)$$

To quantify the contribution of every point $\mathbf{x} \in \mathbb{R}^d$ attached to S_i (resp. S_j) to its collision with S_j (resp. S_i), we can measure the duration of its trajectory that collides with S_j (resp. S_i):

$$f_{S_i}(\mathbf{x}) \triangleq \int_0^1 \mathbf{1}_{S_{j,i}(t)}(\mathbf{x}) dt = \int_0^1 \mathbf{1}_{S_j}(\tau_{j,i}\mathbf{x}) dt, \quad \forall i \neq j \quad (6)$$

To eliminate the contribution of the points that are outside each shape, we can multiply by the indicator functions of each shape:

$$\bar{f}_{S_i}(\mathbf{x}) \triangleq \int_0^1 \mathbf{1}_{S_j}(\tau_{j,i}\mathbf{x})\mathbf{1}_{S_i}(\mathbf{x}) dt, \quad \forall i \neq j \quad (7)$$

To derive global measures (a single value for each solid) from the above local measures, we can integrate them over the respective solids:

$$q_{S_i} \triangleq \int_{S_i} f_{S_i}(\mathbf{x}) d\mu^d[\mathbf{x}] = \int_{\Omega_i} \bar{f}_{S_i}(\mathbf{x}) d\mu^d[\mathbf{x}], \quad \forall i \quad (8)$$

The goal of collision-free co-design is to find set of collision-free solids $S_i \subseteq \Omega_i, \forall i$, in a sense that we shall define precisely below, such that $q_{S_i} = q_{S_j} = 0, \forall i \neq j$, which is true iff for all $\mathbf{x} \in \mathbb{R}^d, \bar{f}_{S_i}(\mathbf{x}) = \bar{f}_{S_j}(\mathbf{x}) = 0, \forall i \neq j$.

2.2. Discretized Formulation

The collision measures discussed in Section 2.1 are representation-agnostic and various representation schemes (e.g., B-reps, mesh, and voxels) can be used as long as they support evaluation d-integrals presented in (6)-(8). Since we plan to use the same representation TO, where we discretize the domain into uniform grid elements. Similar to the formulation presented in [9], we employ an asymmetric discretization strategy where the stationary solid (i.e., the one to which the frame of reference is attached) is discretized via a finite volume scheme, while the moving solid (i.e., the one whose motion is observed) is discretized via a finite sample scheme. In other words, given a sufficiently fine discretization (i.e., edge length of $\epsilon > 0$), we use the the primal grid nodes (i.e., vertices of the finite elements v_j) for the moving part j and the dual grid cells (i.e., finite elements e_i) for the stationary part i . Let $\mathbf{x}_i \in \mathbb{R}^d$ be the coordinates of the i^{th} vertex (i.e., 0-cell) on the grid and $C_i \subset \mathbb{R}^d$ denote the dual

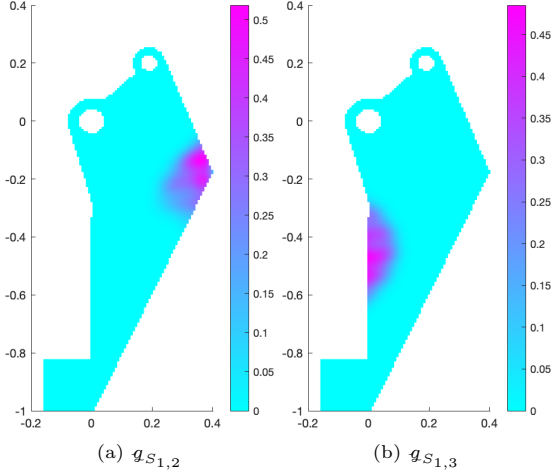


Figure 2: Pair-wise collision fields for the gripper and the two cams.

d-cell (e.g., congruent quadrilateral elements in 2D and hexahedral voxels in 3D), we can define:

$$C_i \triangleq \{\mathbf{x}_i + \mathbf{x} \mid \mathbf{x} \in C\}, \quad C \triangleq [-\epsilon/2, +\epsilon/2]^d \quad (9)$$

Figure 2 illustrates the pair-wise collision fields for the gripper with each of the two cams.

The finite approximations of the collision measure in (8) can be written as matrix equations:

$$\mathbf{g}_{S_{i,j}} \approx [\rho_i^e]^\top [w_{i,j}] [\rho_j^v], \quad (10)$$

The two arrays $[\rho_i^e]_{n_i^e \times 1}$ and $[\rho_j^v]_{n_j^v \times 1}$ are discrete representations of the two solids, i.e., the *design variables*. n_i^e and n_j^v denote the number of elements in solid i and the number of vertices in solid j . The collision weight matrix (CWM) $[w_{i,j}]_{n_i^e \times n_j^v}$ essentially captures the *pairwise correlations* between primal grid nodes of a moving grid and dual grid cells of a stationary grid, which depend solely on the relative motion of the grids and the grid structure.

Assuming small deformations, the CWM *only* depends on the initial designs and needs to be computed only once. We leverage this property in the iterative co-design optimization in Section 3 to ensure scalability of the approach as computing the collision measures a few hundred times for arbitrarily complex shapes and motions can become computationally prohibitive. The CWM computes the aggregate collision between two discretized models over time. The time integral can be approximated using a Reimann sum:

$$w^{i,j} \approx \epsilon^d \delta_t \sum_{k=1}^K \mathbf{1}_{C_i}(\tau_{i,j}(t_k) \mathbf{x}_j), \quad (11)$$

where we consider uniform discretization of the time period $[0, 1]$ into K steps, $t_k \triangleq (k-1)\delta_t$ for $k = 1, 2, \dots, K$, assuming each time step δ_t is small enough to capture the motion trajectories accurately enough.

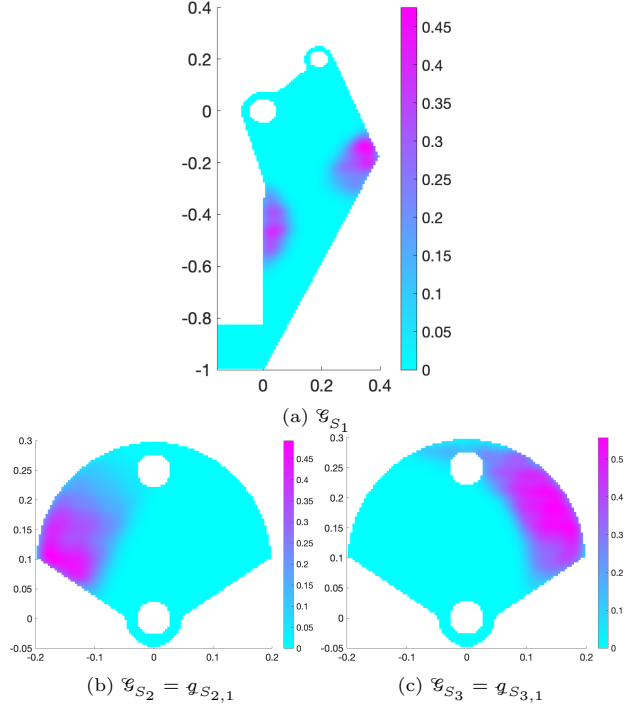


Figure 3: Overall collision fields over the Gripper and two cams. Since the two cams only collides with the gripper, their overall collision field is similar to the their pair-wise collision field with the gripper.

The collision measure of (10) can be generalized for multiple parts as:

$$\mathcal{G}_i \approx \sum_{i \neq j} [\rho_i^e]^\top [w_{i,j}] [\rho_j^v], \quad (12)$$

Figure 3 illustrates the overall collision fields for the gripper (\mathcal{G}_{S_1}) and the two cams (\mathcal{G}_{S_2} and \mathcal{G}_{S_3}). In this scenario, there is no collision between the cams and the overall collision is identical to their pair-wise collision field with only the gripper.

2.3. Collision Sensitivity Analysis

To enable efficient co-design optimization $[\rho_i^e]_{n_i^e \times 1}$ while avoiding collisions, the collision measures of (12) must be differentiated with respect to the design variables $[\rho_i^e]$. The resulting discrete sensitivity fields are computed using a chain rule:

$$\left[\frac{\partial \mathcal{G}_i}{\partial \rho_i^e} \right] \approx \sum_{i \neq j} [w_{i,j}] [\rho_j^v], \quad (13)$$

Since we aim to remove material from regions with higher collision measure values, we define:

$$\mathcal{T}_{\mathcal{G}_i} := 1 - \left[\frac{\partial \mathcal{G}_i}{\partial \rho_i^e} \right]. \quad (14)$$

Figure 4 illustrates the overall sensitivity fields for the assembly of Figure 20.

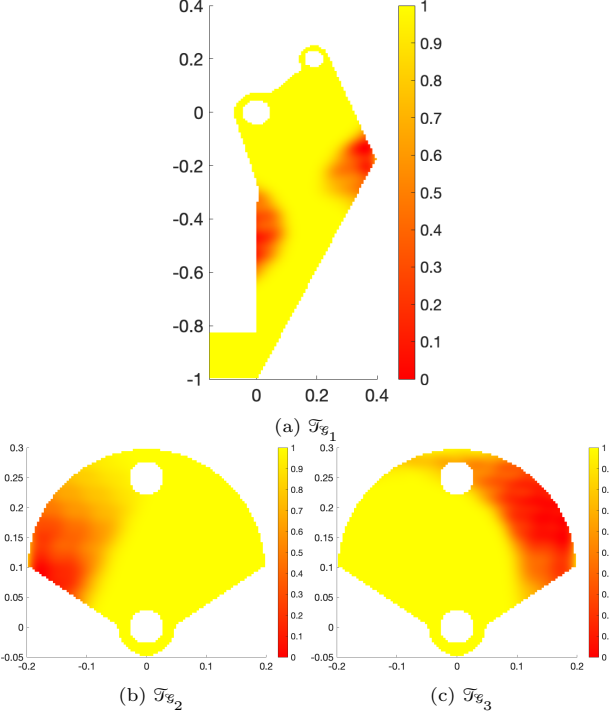


Figure 4: Collision gradient fields over the Gripper and two cams.

3. Co-Design Optimization

In this section, we present the TO formulation to enable co-design of moving components of an assembly. To this end, we employ the Pareto-tracing TO (PareTO) [20] to explore the trade-offs between competing objectives, here compliance and collision avoidance. At every step, we conduct a fixed-point iteration to find a local optimum at each volume fraction. The optimization terminates after all collisions are resolved.

Mathematically, we formulate the optimization problem as finding $[\rho_i^e] \subseteq \Omega_i$, $i = 1, \dots, N$ to:

$$\text{Find } [\rho_i^e] \subseteq \Omega_i : \begin{cases} \text{select target } \bar{V}_i^{\text{targ}} \in (0, 1], \forall i \\ \text{ILL: } \begin{cases} \text{minimize } f(\rho_i^e), \\ \text{s.t. } [\mathbf{K}_i][\mathbf{u}_i] = [\mathbf{f}_i], \\ \bar{V}_i = \bar{V}_i^{\text{targ}}, \\ \mathcal{G}_i = 0, \forall i. \end{cases} \end{cases} \quad (15)$$

Generally, we begin the optimization process with all solid designs are gradually reduce the target volume fraction through $\bar{V}_i^{\text{targ}} \leftarrow \bar{V}_i^{\text{targ}} - \delta_{v_i}$. To be able to effectively explore the design spaces (from extreme cases where material is removed only from one part to intermediate scenarios where material is removed from all part with various levels of aggressiveness), we define $\delta_{v_i} \triangleq \gamma \delta_v^{\text{max}}$; where δ_v^{max} is the maximum allowable volume decrement for all parts and the hyper-parameter $0 \leq \gamma \leq 1$ is used to control the decrement aggressiveness for each component.

The inner-loop optimization can be expressed as local minimization of the Lagrangian defined as:

$$\mathcal{L}_i := [\mathbf{f}_i]^T[\mathbf{u}_i] + [\mu_i]^T \left([\mathbf{K}_i][\mathbf{u}_i] - [\mathbf{f}_i] \right) + \lambda_{v_i}(\bar{V}_i - \bar{V}_i^{\text{targ}}) + \lambda_{g_i} \mathcal{G}_i. \quad (16)$$

The Karush–Kuhn–Tucker (KKT) conditions [21] for this problem are given by $\nabla_{\rho_i^e} \mathcal{L} = 0$ in which the gradient is defined by partial differentiation with respect to the independent variables; namely, the design variables used to represent $[\rho_i^e]$ and the Lagrange multipliers μ_i , λ_{v_i} and λ_{g_i} . The latter simply encodes the constraints into $\nabla_{\rho_i^e} \mathcal{L} = 0$:

$$\frac{\partial}{\partial \mu_i} \mathcal{L}_i = [\mathbf{K}_i][\mathbf{u}_i] - [\mathbf{f}_i] := [0], \quad (17)$$

$$\frac{\partial}{\partial \lambda_{v_i}} \mathcal{L}_i = (\bar{V}_i - \bar{V}_i^{\text{targ}}) := 0, \quad (18)$$

$$\frac{\partial}{\partial \lambda_{g_i}} \mathcal{L}_i = \mathcal{G}_i := 0, \quad (19)$$

Next, let the prime symbol $(\cdot)'$ represent the generic (linear) differentiation of a function with respect to ρ_i^e , we obtain (via chain rule):

$$\mathcal{L}_i' = [\mathbf{f}_i]^T[\mathbf{u}_i'] + [\mu_i]^T \left([\mathbf{K}_i][\mathbf{u}_i] \right)' + \lambda_{v_i} \bar{V}_i' + \lambda_{g_i} \mathcal{G}_i', \quad (20)$$

Using the adjoint method [22], we have $[\mu_i] := -[\mathbf{K}_i]^{-1}[\mathbf{f}_i]$. Thus, (20) reduces to:

$$\mathcal{L}_i' = \lambda_{v_i} \bar{V}_i' \underbrace{-[\mathbf{u}_i]^T[\mathbf{K}_i'][\mathbf{u}_i]}_{\text{compliance sensitivity}} + \lambda_{g_i} \underbrace{\mathcal{G}_i'}_{\text{collision sensitivity}} \quad (21)$$

In this work, we use the TSF interpretation for the compliance sensitivity in (21). The topological sensitivity $\mathcal{T}(\mathbf{x})$ is defined as the ratio of the first-order change in the objective f to the area (or volume) of the *hypothetical* infinitesimal hole $B_\epsilon(\mathbf{x})$ in the design at point \mathbf{x} , as illustrated in 5. Mathematically,

$$\mathcal{T}_{\mathbf{x}}(f) \equiv \lim_{\epsilon \rightarrow 0^+} \frac{f(\Omega - B_\epsilon(\mathbf{x})) - f(\Omega)}{-\text{vol}(B_\epsilon(\mathbf{x}))}, \quad (22)$$

where $\text{vol}(\cdot)$ denotes the volume (or area in 2D) of the inclusion.

The closed-form expression for the topological derivative of compliance for plane-stress problems in 2D is [23]:

$$\mathcal{T}_{\mathbf{x}}(f) = \frac{4}{1 + \nu} \sigma : \varepsilon - \frac{1 - 3\nu}{1 - \nu^2} \text{tr}(\sigma) \text{tr}(\varepsilon), \quad (23)$$

where ν , σ , and ε respectively denote the Poisson's ratio, stress tensor, and strain tensor at every point \mathbf{x} . Similar closed-form expressions have also been derived for 3D linear elasticity problems [24].

Neglecting the topological sensitivity for volume (constant everywhere), we have the following expression for the overall TSF for each part with $[\rho_i^e]$ as design variables:

$$\hat{\mathcal{T}}_i := \mathcal{T}(\mathcal{L}_i) = \mathcal{T}_i + \lambda_{g_i} \mathcal{T}_{\mathcal{G}_i} \quad (24)$$

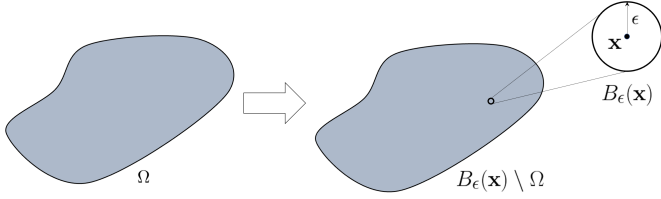


Figure 5: Computing the topological sensitivity by hypothetically perturbing the design Ω at point \mathbf{x} via a small inclusion of radius ϵ .

At every step, we perform FEA, compute sensitivity field, and reject a few elements with *lowest* compliance sensitivity value and repeat until we satisfy the collision-free constraint. Consider now a domain $S_i^{\tau_i}$ as the set of all points in part i where the sensitivity field exceeds the value τ_i , defined per:

$$S_i^{\tau} \triangleq \{\mathbf{x} \mid \hat{\mathcal{G}}_{\mathbf{x}} > \tau_i\} \quad (25)$$

The value of λ_{g_i} can be adaptively adjusted throughout the optimization considering the values of compliance and violation of collision constraints. Here, we prescribe the value of λ_{g_i} to explore the feasible design space and provide more insight on the impact of collision-avoidance constraint.

Figure 6 illustrates the optimized designs for the gripper and the two cam structures at volume fraction $v_i = 0.5$ (for all) *without* incorporating the collision avoidance constraint. We consider $\delta v^{max} = 0.01$ and $\gamma_i = 1$ for all parts. Observe that in by solely optimizing the components with respect to compliance, the parts collide with each other on multiple occasions throughout their prescribed trajectories (red regions in Figures 6b, 6d, and 6f).

Algorithm 1 provides a description of the approach.

4. Results

In this section, we demonstrate the effectiveness of the proposed approach through a few examples with various design complexities and motions. For all examples, we assume Young's modulus $E = 1 \text{ GPa}$, Poisson's ratio $\nu = 0.3$, and maximum volume decrement $\delta v = 0.025$. All examples are run on a MacBook Pro M1 Max with 32 GB of memory.

4.1. Cam and Follower

The first example is the cam-follower system of Figure 7 with the dimensions and initial positions shown in Figure 9. The cam is prescribed to rotate 2π radians about the center of its circular cutout hole, which is located at $O_C = [0, 8]$ of the space, while the follower moves in the vertical direction as a function of the angular position of the cam, θ_C . The vertical position y_F of the center of the follower, as a function of θ_C provided by the following formula:

$$y_F = \frac{3L}{4} + \frac{L}{8} \cos(2\theta_C). \quad (26)$$

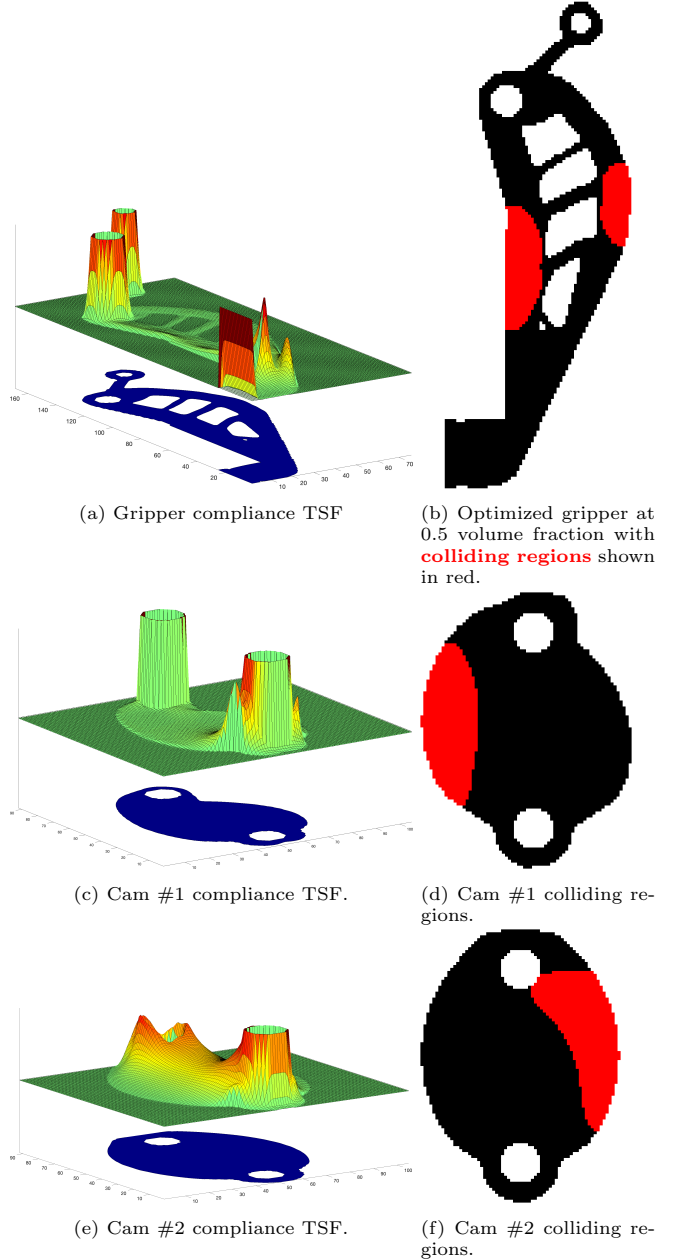


Figure 6: Optimized designs at 0.7 volume fraction for all components *without* considering collision avoidance constraint ($\lambda_{g_i} = 0, \forall i$).

The temporal resolution for collision analysis is 1000 time steps. The follower and the cam are discretized into 10,000 and 20,000 bilinear quadrilateral finite elements, respectively. The boundary conditions (BC) for the follower is illustrated in Figure 8a, where we assume fixed degrees of freedom (DOF) along the y axis at the bottom-left corner and fixed DOFs in both x and y at the bottom-right corner. An external force $f_{ext}^F = [1, 0]$ is applied at the top-left corner. Figure 8b illustrates the BC for the square cam, where the circular cutout hole is assumed fixed and an external force $F_{ext}^C = [0, -1]$ is applied at the right-top corner. Figure 9 shows the initial collision measure fields for the two

Algorithm 1 Co-Design via Collision-Aware PareTO

```

1: procedure PARETO( $\Omega_i, V^*, \delta v, \gamma_i$ )
2:    $[\rho_i^e] \leftarrow \Omega_i$   $\triangleright$  Initialize at volume fraction 1.0
3:    $V_i \leftarrow \text{EVALUATEVOLUME}([\rho_i^e])$ 
4:    $\lambda_{g_i} \leftarrow \gamma_i \delta v$ 
5:   while  $V_i > V^*$  and  $\mathcal{G}_i > 0, \forall i$  do
6:      $v_i \leftarrow V_i - \delta v_i$ 
7:      $\mathbf{u}_i \leftarrow \text{SOLVEFEA}([\rho_i^e], \mathbf{K}_i, \mathbf{f}_i)$ 
8:      $f \leftarrow \text{EVALUATECOMPLIANCE}([\rho_i^e], \mathbf{u}_i)$ 
9:      $\mathcal{G}_i \leftarrow \text{EVALUATECOLLISION}([\rho_i^e], [\rho_j^v] \forall i, j)$ 
10:     $\delta f \leftarrow 1$ 
11:    while  $\delta f > \epsilon$  do
12:       $\mathcal{G}_i \leftarrow \text{EVALUATECOLLISION}([\rho_i^e], [\rho_j^v], \forall i, j)$ 
13:       $\mathcal{T} \leftarrow \text{COMPLIANCEGRADIENT}([\rho_i^e], \mathbf{u}_i)$ 
14:       $\mathcal{T}_{\mathcal{G}_i} \leftarrow \text{COLLISIONGRADIENT}([\rho_i^e], [\rho_j^v])$ 
15:       $\hat{\mathcal{T}} \leftarrow \mathcal{T}_i + \lambda_{g_i} \left[ \frac{\partial \mathcal{G}_i}{\partial \rho_i^e} \right]$ 
16:       $\tau_i \leftarrow \text{FINDTHRESHOLD}([\rho_i^e], \hat{\mathcal{T}}, \delta v)$ 
17:       $[\rho_i^e]^* \leftarrow \text{EXTRACTLEVELSET}(\hat{\mathcal{T}}, \tau)$ 
18:       $\mathbf{u}_i \leftarrow \text{SOLVEFEA}([\rho_i^e]^*, \mathbf{K}_i, \mathbf{f}_i)$ 
19:       $f^* \leftarrow \text{EVALUATECOMPLIANCE}([\rho_i^e]^*, \mathbf{u}_i)$ 
20:       $\delta f \leftarrow |f^* - f|$ 
21:       $f \leftarrow f^*$ 
22:    end while
23:     $[\rho_i^e] \leftarrow [\rho_i^e]^*$ 
24:     $V_i \leftarrow \text{EVALUATEVOLUME}([\rho_i^e])$ 
25:  end while
26:  return  $[\rho_i^e]$ 
27: end procedure

```

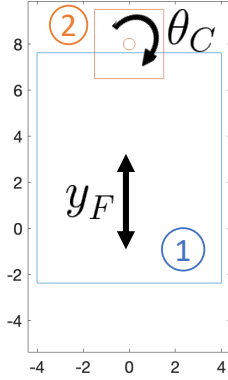


Figure 7: Cam and follower initial configuration.

components under the prescribed trajectories, which results in the initial collision regions of Figure 10. Figure 13 shows the compliance TSF, collision gradient field, and the augmented sensitivity fields for both the cam and the follower with $\lambda_{g_1} = \lambda_{g_2} = 0.5$. Observe that removing material solely based on the collision gradient would removed critical regions where Dirichlet or Neumann BC are applied as demonstrated in Figures 11a and 11b, where we only optimize the cam geometry *without* considering compliance. In other words, the optimization reduces to find-

ing the follower unsweep as the cam shape, which is *not* a valid design from the compliance perspective ($f_C \rightarrow \infty$). The evolution of collision volume for the follower and the cam are shown in Figure 12.

On the other hand, TSF alone does not capture information about collision and is unlikely to produce a collision-free assembly. However, the augmented sensitivity field encapsulates information about both constraints and will successfully result in collision-free and physically valid assemblies. Figures 11c and 11d illustrate the co-optimized cam-follower assembly for $\lambda_{g_1} = \lambda_{g_2} = 0.2$, $\gamma_1 = 1$, and $\gamma_2 = 0.5$. Alternatively, Figures 11e and 11f show the co-optimized parts for $\lambda_{g_1} = \lambda_{g_2} = 0.2$, $\gamma_1 = 0.25$, and $\gamma_2 = 1$. Table 1 summarizes the results for the optimized cam-follower systems with different parameters λ_{g_i} and γ_i .

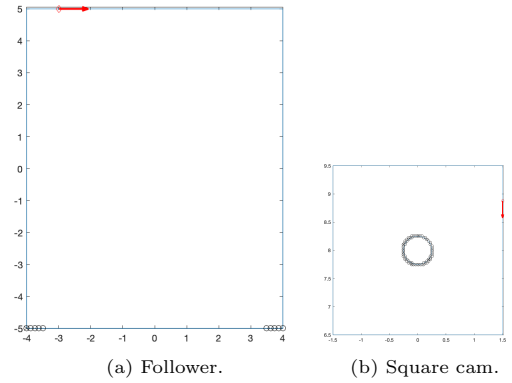


Figure 8: Cam and follower boundary conditions.

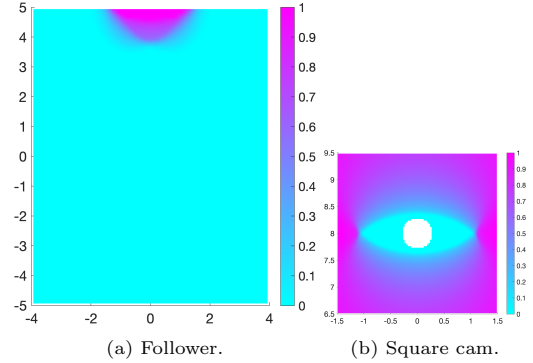


Figure 9: Initial collision measure fields for the cam-follower system.

4.2. Three Squares Assembly

As the second example, let us consider the three-body system of Figure 14, where $\theta_1 = [\pi/2, \pi/5]$, $\theta_2 = [0, 3\pi/10]$, $\theta_3 = [\pi/2, -3\pi/2]$ with 500 steps temporal resolution for collision analysis. The design domains and their corresponding boundary conditions are shown in fig. 15, where all designs are assumed to be fixed at the center hole. The external forces are applied at top-middle points with $f_{ext}^1 = [1, 0]$, $f_{ext}^2 = [1, 1]$, and $f_{ext}^3 = [-1, 1]$. All designs are discretized into 6,000 elements.

Table 1: Impact of γ_i and λ_{g_i} on compliance and collision for the cam-follower system.

λ_{g_i}	γ_1	γ_2	v_1	v_2	f_1/f_1^0	f_2/f_2^0	\mathcal{G}_1	\mathcal{G}_2
1	0	1	1.00	0.08	1.00	∞	0.00	0.00
1	1	0	0.93	1.00	1.10	1.00	0.00	0.00
0.05	1	1	0.90	0.90	1.02	1.01	0.00	0.00
0.2	1	1	0.90	0.90	1.05	1.01	0.00	0.00
0.5	1	1	0.90	0.90	1.05	1.01	0.00	0.00
0.2	1	0.5	0.90	0.95	1.05	1.00	0.00	0.00
0.2	0.5	1	0.91	0.83	1.05	1.01	0.00	0.00
0.2	0.25	1	0.93	0.70	1.05	1.04	0.00	0.00
0.2	1	0.25	0.90	0.98	1.05	1.00	0.00	0.00

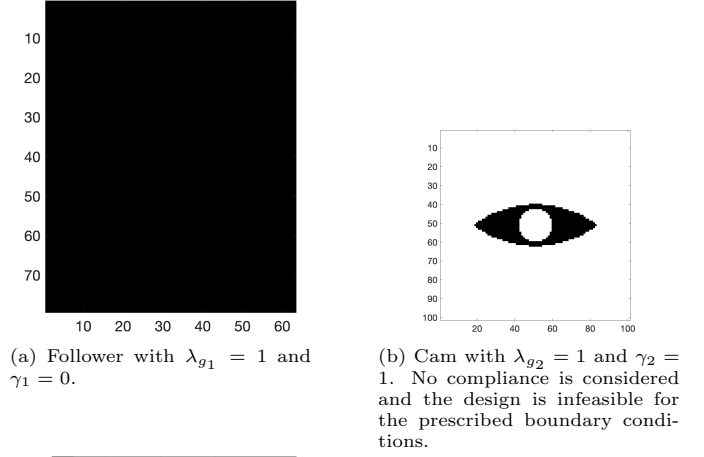
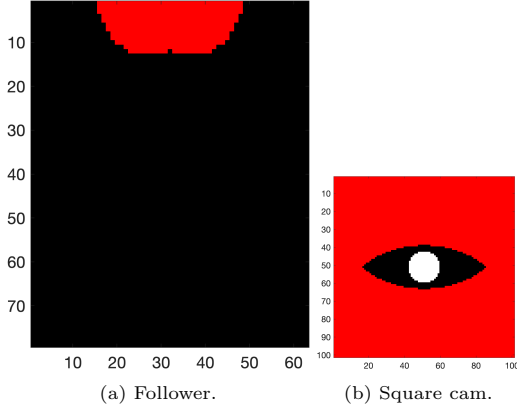


Figure 10: Initial colliding regions for the cam-follower system.

Figure 16 illustrates the pair-wise collision measure fields and the overall collision measure fields for the initial domains. To demonstrate the impact of volume decrement on the final assembly, Figure 17 shows the co-optimized system considering three different scenarios, 1) $\gamma_1 = 1, \gamma_2 = 0.5, \gamma_3 = 0.25$, 2) $\gamma_1 = 0.5, \gamma_2 = 0.25, \gamma_3 = 1$, and 3) $\gamma_1 = 1, \gamma_2 = 1, \gamma_3 = 1$. The final volume fractions and compliance values are summarized in Table 2.

Figure 18 shows the collision-free motion of the co-optimized system for the first scenario at six different snapshots. The evolution of compliance and collision volume for all components are illustrated in Figure 19.

4.3. Gripper and Cams Assembly

Next, let us revisit the system of Figure 1a comprising a gripper and two cams with $\theta_1 = [0, \pi/2]$, $\theta_2 = [0, \pi]$, $\theta_3 = [\pi/2, -3\pi/2]$. The temporal resolution is 500 time steps and all components are discretized into 6,000 finite elements. The boundary conditions are shown in Figure 20.

Let us consider a case with $\lambda_{g_i} = 0.5$ and $\gamma_i = 1$ for all components. We reach a collision-free configuration at volume fraction of 0.6 for all designs. Figures 21a, 21c, and 21e illustrate the final augmented sensitivity field and the corresponding level-sets, which gives the iso-surfaces of the optimized designs. Figures 21b, 21d, and 21f show the optimized grids. The optimized gripper has $f_1/f_1^0 = 1.30$

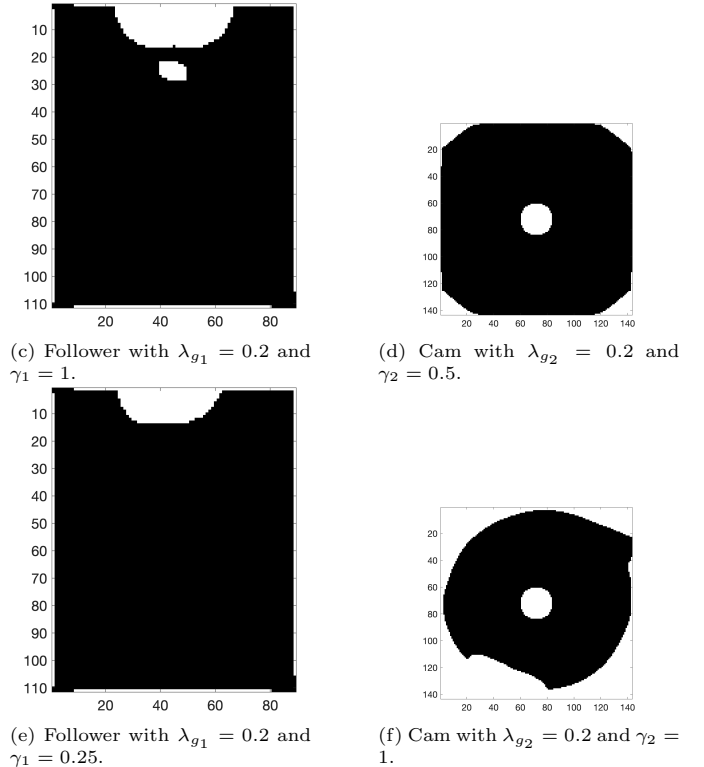


Figure 11: Co-optimized cam-follower system with different parameters.

Table 2: Impact of γ_i on compliance and collision for the three-body system.

γ_1	γ_2	γ_3	v_1	v_2	v_3	f_1/f_1^0	f_2/f_2^0	f_3/f_3^0	\mathcal{G}_1	\mathcal{G}_2	\mathcal{G}_3
1	1	1	0.40	0.40	0.40	1.06	1.07	1.17	0.00	0.00	0.00
0.5	0.25	1	0.40	0.70	0.30	1.05	1.01	1.36	0.00	0.00	0.00
1	0.5	0.25	0.40	0.70	0.85	1.06	1.01	1.04	0.00	0.00	0.00

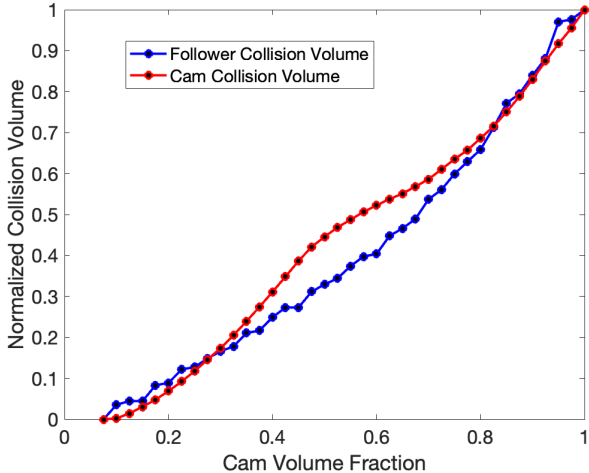


Figure 12: The evolution of collision volume between the cam and the follower without considering compliance ($\lambda_{g_1} = \lambda_{g_2} = 0$) and only removing material from the cam ($\gamma_1 = 0$ and $\gamma_2 = 1$). The final cam geometry is similar to follower unsweep.

with maximum deformation of $1.7e-4$ (m) and maximum von Mises stress of 0.88 (MPa). The two optimized cams have $f_2/f_2^0 = 1.02$ and $f_3/f_3^0 = 1.03$. The optimized cam 1 has maximum deformation of $1.1e-6$ (m) and maximum von Mises stress of $1.3e-5$ (MPa). The optimized cam 2 has maximum deformation of $6.4e-8$ (m) and maximum von Mises stress of $1.9e-6$ (MPa). Figure 22 shows the collision-free motion of the optimized design at multiple snapshots.

Table 3 summarizes the computation time for the gripper and cams example for the entire optimization process. Observe that the majority of the computation time is spent on evaluating the physical performance of the parts and FEA remains the bottleneck. The one-time computation of the CWMs takes about 18 seconds at the pre-processing stage. On the other hand, the evaluation of the collision measures during the optimization loop relies on fast matrix multiplications and only takes about 1 second in total, while compliance gradient computation takes about 8 seconds.

4.4. Three-Body System in 3D

Finally, let us consider the three-body system of Figure 23 in three dimensions. The loading conditions and domain sizes are depicted in Figure 24. The parts are discretized as following, 1) $35 \times 25 \times 10$, 2) $20 \times 20 \times 20$, and 3) $30 \times 10 \times 30$. The first part rotates about the x axis with angle $\theta_1 = [\pi, 1.1\pi]$. The second part is also rotating

Table 3: Computation times in seconds.

Operation	Time (s)
FEA	88.43
Compliance Gradient	8.01
Collision Weights (pre-process)	18.05
Collision Measure	1.09
Overall	121.75

about the x axis with angle $\theta_2 = [0, 0.1\pi]$ with its center at $[35, 5, 30]$. And the third part is first re-aligned by a 90° rotation about z axis and then rotated about y axis with angle $\theta_3 = [0, 0.1\pi]$ with its center at $[15, 20, 15]$. The temporal resolution is 100 time steps.

Figure 25 illustrates the overall collision fields for all three components. Assuming $\lambda_{g_i} = 0.5$, $\forall i$ and $\gamma_i = 1$, $\forall i$, Figure 26 shows the co-optimized structures at 0.3 volume fraction. Figure 27 illustrates the evolution of compliance and collision volume for each component.

5. Conclusions

In this paper, we presented a TO formulation for simultaneously co-optimizing multiple components within an assembly. The method is based on a locally differentiable measure of aggregate pair-wise collision between moving parts. To efficiently explore the feasible design space, we have extended the Pareto-tracing TO, where we augment the compliance sensitivity field with the collision gradient and gradually remove material to co-generate high-performance, light-weight, and collision-free structures.

Regarding the design for assembly, our work extends the application of TO beyond the design of individual parts to encompass assembly-level design, where both parts and components are designed concurrently to achieve physics-based goals while also ensuring that parts do not collide.

In the present work, we have assumed that the pairwise collision between parts does not occur between functional surfaces, i.e., at least one of the parts can be modified to avoid collision. The proposed work focused on compliance as the performance objective. Future work will extend the current framework to consider local measures, such as stress [25, 26]. Future work will also incorporate inertia constraints, dynamic contact loads, and collision-avoidance under large deformations. Another possible extension to our co-design framework is to simultaneously optimize the shapes of parts and their relative motions using differentiable collision measures provided by collision detection surrogate models [27–29].

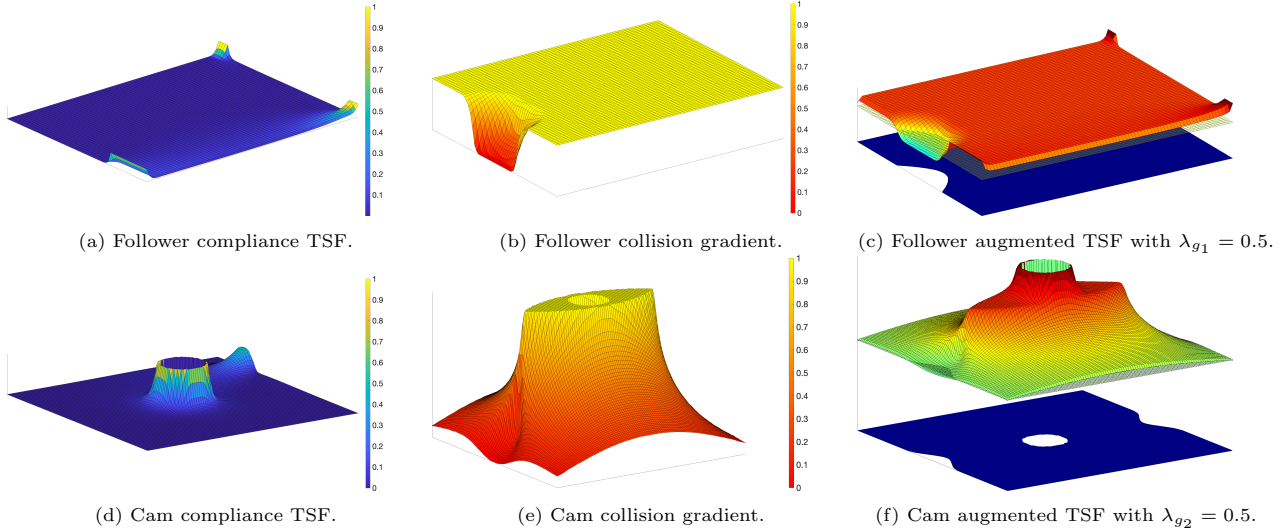


Figure 13: Cam-follower augmented TSFs with $\lambda_{g_i} = 0.5$ with the level-set at 0.025 decrement.

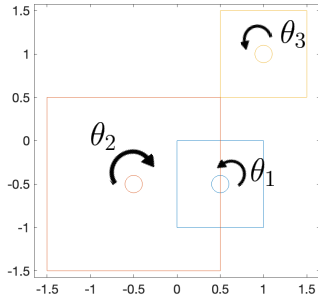


Figure 14: Cam and follower initial configuration.

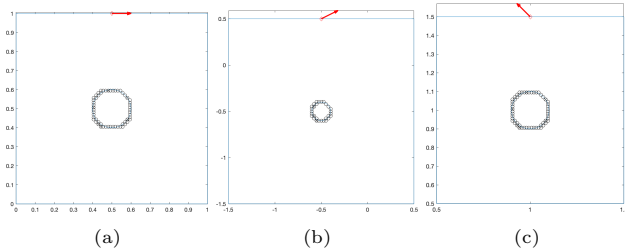


Figure 15: Three rotating-body boundary conditions.

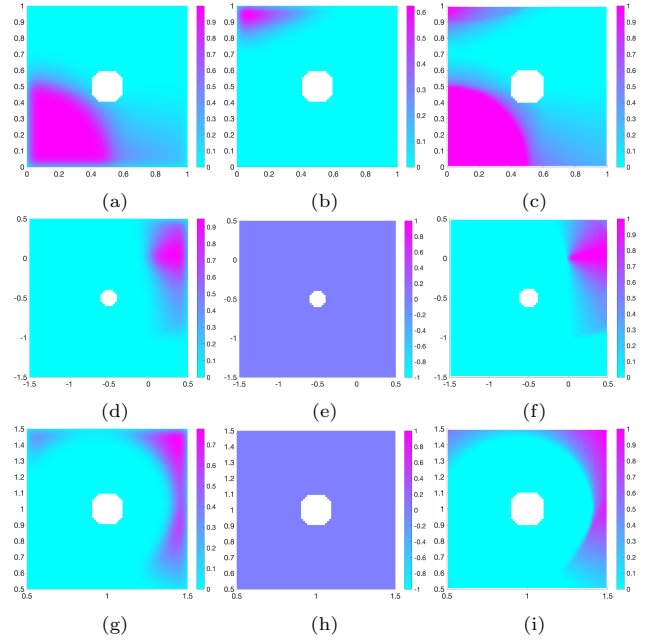


Figure 16: Three rotating-body initial pair-wise and overall collision measure fields.

Acknowledgments

This research was developed with funding from the Xerox Corporation. The views, opinions and/or findings expressed are those of the authors and should not be interpreted as representing the official views or policies of the Xerox Corporation.

References

[1] H. Li, T. Kondoh, P. Jolivet, K. Furuta, T. Yamada, B. Zhu, K. Izui, S. Nishiwaki, Three-dimensional topology optimization of a fluid-structure system using body-fitted mesh adaption based on the level-set method, *Applied Mathematical Modelling* 101 (2022) 276–308.

[2] A. M. Mirzendehtdel, M. Behandish, S. Nelaturi, Topology optimization with accessibility constraint for multi-axis machining, *Computer-Aided Design* 122 (2020) 102825.
[3] J. Liu, A. T. Gaynor, S. Chen, Z. Kang, K. Suresh, A. Takezawa, L. Li, J. Kato, J. Tang, C. C. Wang, et al., Current and future trends in topology optimization for additive manufacturing, *Structural and multidisciplinary optimization* 57 (2018) 2457–2483.
[4] S. Guanghui, G. Chengqi, Q. Dongliang, W. Dongtao, T. Lei, G. Tong, An aerospace bracket designed by thermo-elastic topology optimization and manufactured by additive manufacturing, *Chinese Journal of Aeronautics* 33 (4) (2020) 1252–1259.
[5] D. Jankovics, A. Barari, Customization of automotive structural components using additive manufacturing and topology optimization, *IFAC-PapersOnLine* 52 (10) (2019) 212–217.
[6] N. Wu, S. Li, B. Zhang, C. Wang, B. Chen, Q. Han, J. Wang,

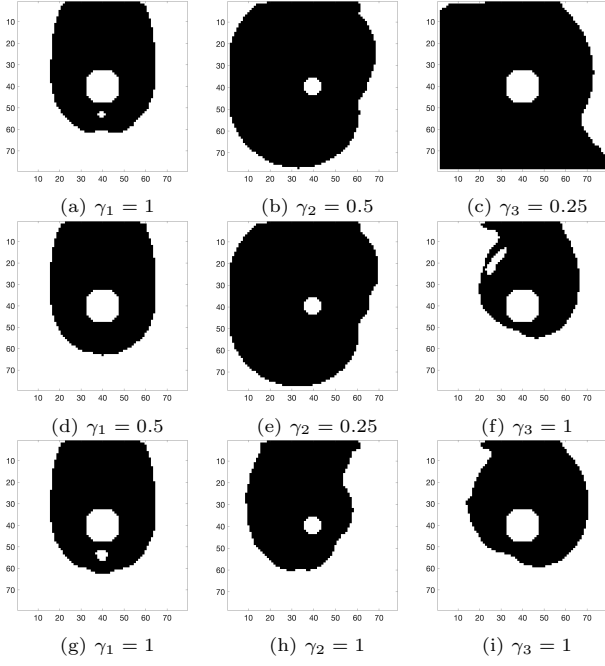


Figure 17: Co-optimized three rotating bodies with different volume decrement ratio γ_i .

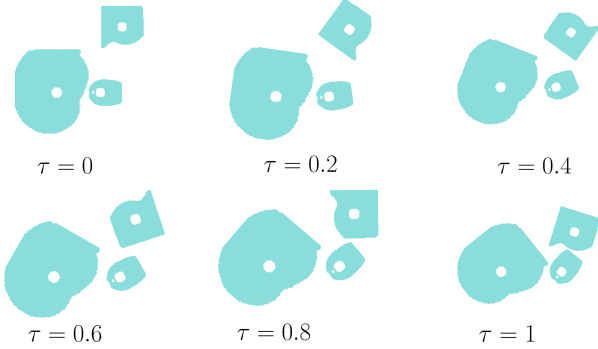


Figure 18: Co-optimized three rotating bodies system with ($\lambda_{g_i} = 0.5$ and $\gamma_1 = 1$, $\gamma_2 = 0.5$, and $\gamma_3 = 0.25$) to simultaneously optimize for stiffness and collision avoidance.

- The advances of topology optimization techniques in orthopedic implants: A review, *Medical & Biological Engineering & Computing* 59 (9) (2021) 1673–1689.
- [7] A. M. Mirzendehtel, K. Suresh, A pareto-optimal approach to multimaterial topology optimization, *Journal of Mechanical Design* 137 (10) (2015).
 - [8] F. Stöckli, K. Shea, Topology optimization of rigid-body systems considering collision avoidance, *Journal of Mechanical Design* 142 (8) (2020) 081705.
 - [9] C. B. Morris, M. Behandish, Co-generation of collision-free shapes for arbitrary one-parametric motion, *Computer-Aided Design* 151 (2022) 103323.
 - [10] A. M. Mirzendehtel, M. Behandish, S. Nelaturi, Exploring feasible design spaces for heterogeneous constraints, *Computer-Aided Design* 115 (2019) 323–347.
 - [11] H. T. Ilies, V. Shapiro, On shaping with motion, *J. Mech. Des.* 122 (4) (2000) 567–574.
 - [12] H. Ilies, V. Shapiro, A class of forms from function: the case of parts moving in contact, *Research in Engineering Design* 13 (3)

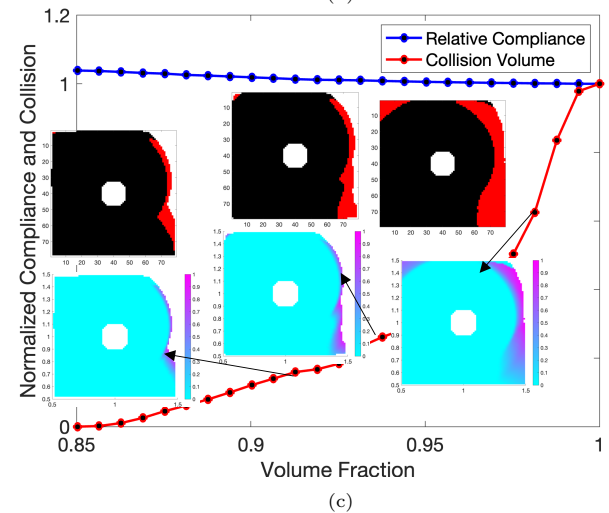
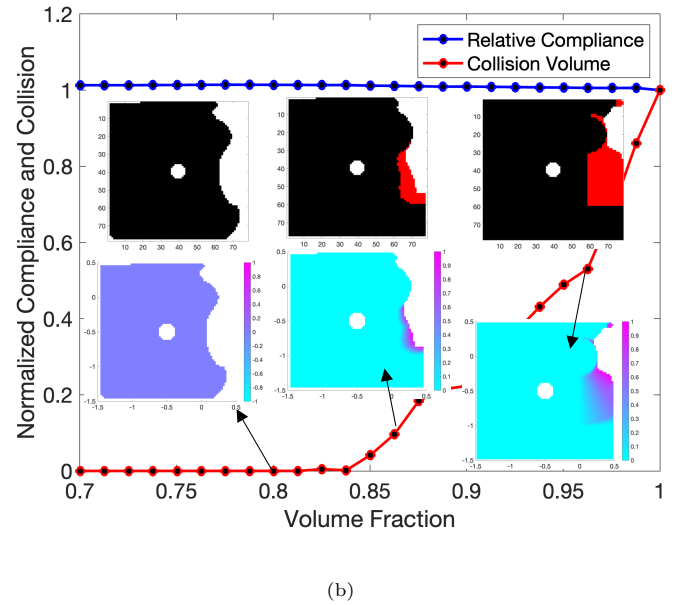
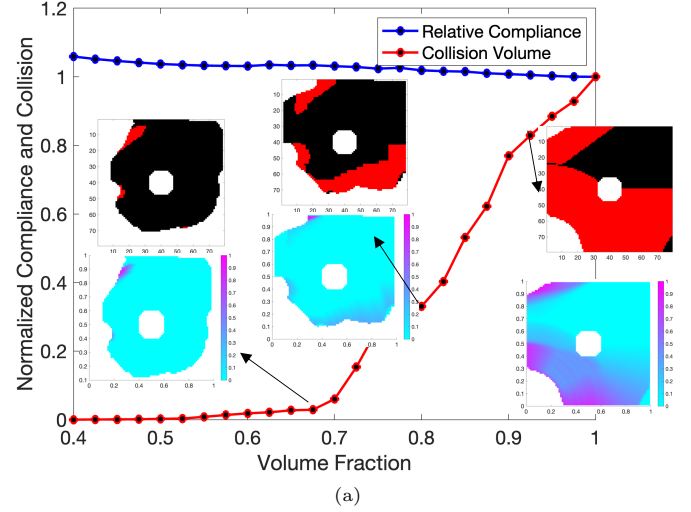


Figure 19: Convergence for co-optimization of the three-body system to a set of collision-free shapes.

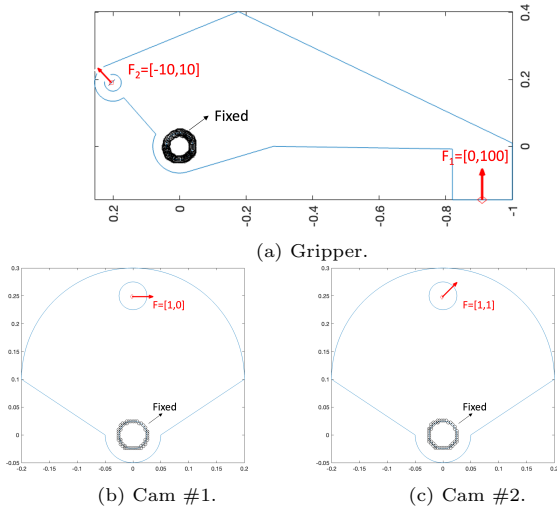


Figure 20: Gripper and two cams boundary conditions.

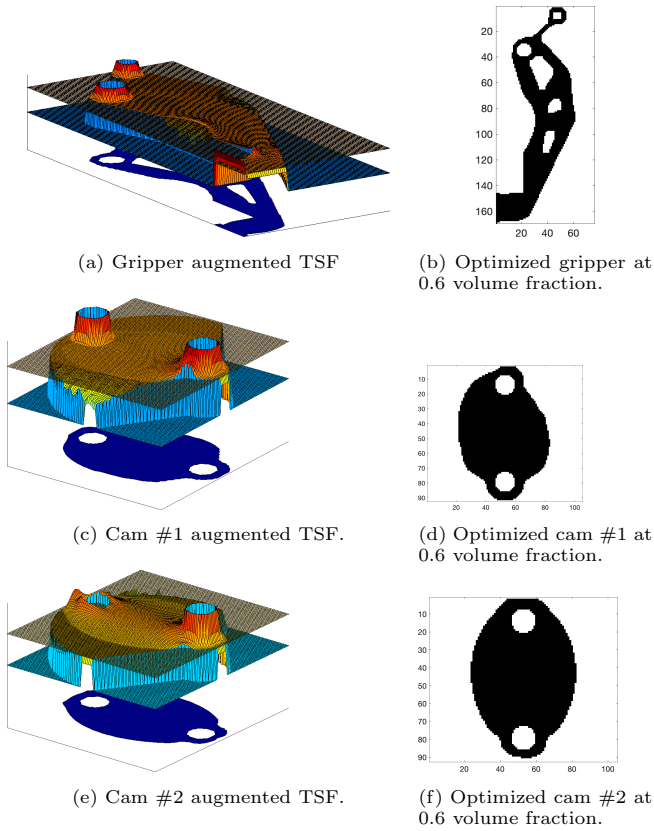


Figure 21: Co-optimized designs at 0.6 volume fraction for all components *with* considering collision avoidance constraint ($\lambda_{g_i} = 0.5$ and $\gamma_i = 1, \forall i$).

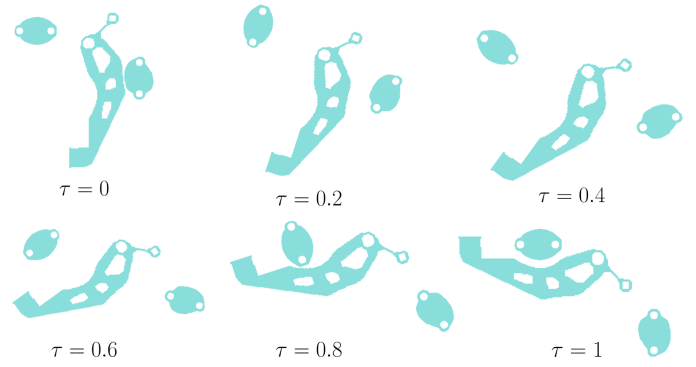


Figure 22: Co-optimized gripper-cams system with ($\lambda_{g_i} = 0.5$ and $\gamma_i = 1, \forall i$) to simultaneously optimize for stiffness and collision avoidance.

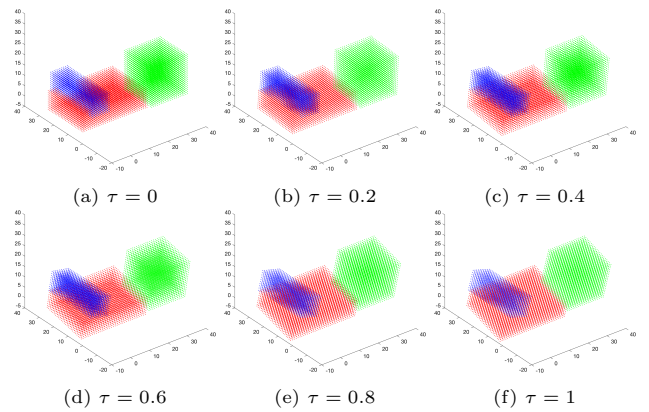


Figure 23: Three-body system motion snapshots.

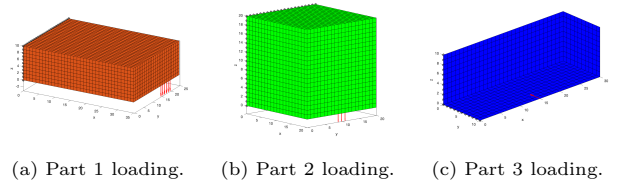


Figure 24: Three-body system boundary conditions.

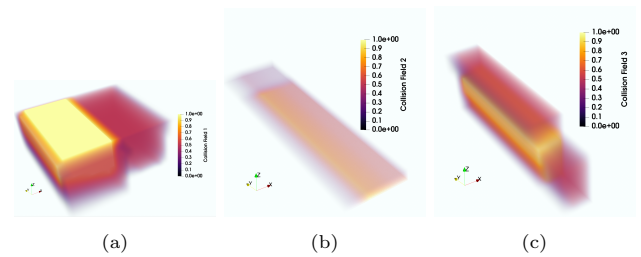


Figure 25: Three-body system collision measure fields.

(2002) 157–166.
 [13] S. Nelaturi, V. Shapiro, Configuration products and quotients in geometric modeling, *Computer-Aided Design* 43 (7) (2011) 781–794.
 [14] M. Lysenko, S. Nelaturi, V. Shapiro, Group morphology with convolution algebras, in: *Proceedings of the 14th ACM symposium on solid and physical modeling*, 2010, pp. 11–22.
 [15] M. Behandish, S. Nelaturi, J. de Kleer, Automated process planning for hybrid manufacturing, *Computer-Aided Design* 102

(2018) 115–127.
 [16] M. Behandish, A. M. Mirzendehtel, S. Nelaturi, A classification of topological discrepancies in additive manufacturing, *Computer-Aided Design* 115 (2019) 206–217.
 [17] S. Nelaturi, M. Behandish, A. M. Mirzendehtel, J. de Kleer, Automatic support removal for additive manufacturing post processing, *Computer-Aided Design* 115 (2019) 135–146.
 [18] A. M. Mirzendehtel, M. Behandish, S. Nelaturi, Optimizing

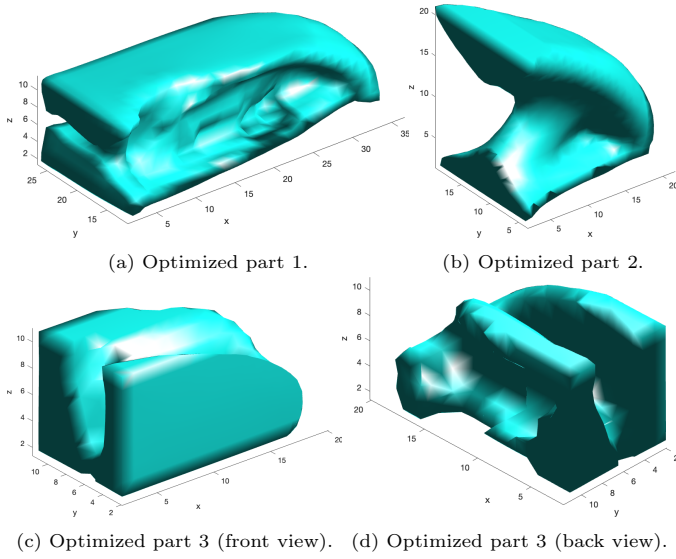


Figure 26: Co-Optimized three-body system at 0.3 volume fraction with $\lambda_{g_i} = 0.5$.

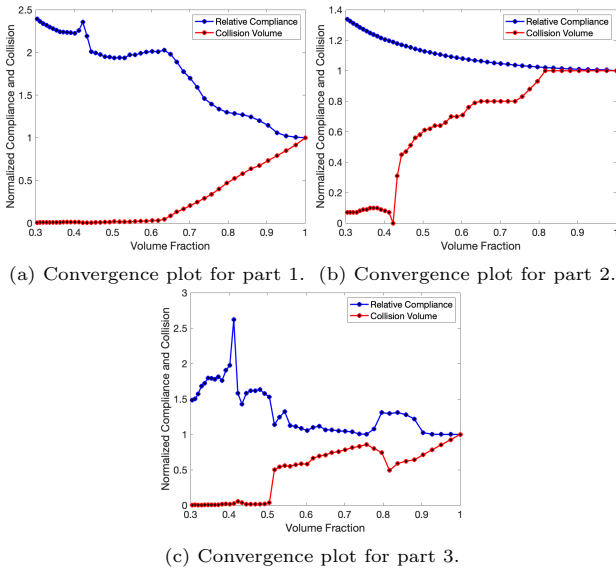


Figure 27: Three-body system convergence plots.

build orientation for support removal using multi-axis machining, *Computers & Graphics* 99 (2021) 247–258.

- [19] A. M. Mirzendehtdel, M. Behandish, S. Nelaturi, Topology optimization for manufacturing with accessible support structures, *Computer-Aided Design* 142 (2022) 103117.
- [20] K. Suresh, A 199-line matlab code for pareto-optimal tracing in topology optimization, *Structural and Multidisciplinary Optimization* 42 (2010) 665–679.
- [21] S. Wright, J. Nocedal, et al., *Numerical optimization*, Springer Science 35 (67-68) (1999) 7.
- [22] M. P. Bendsoe, O. Sigmund, *Topology optimization: theory, methods, and applications*, Springer Science & Business Media, 2003.
- [23] A. A. Novotny, J. Sokołowski, *Topological derivatives in shape optimization*, Springer Science & Business Media, 2012.
- [24] A. Novotny, R. Feijóo, E. Taroco, C. Padra, Topological sensitivity analysis for three-dimensional linear elasticity problem, *Computer Methods in Applied Mechanics and Engineering* 196 (41-44) (2007) 4354–4364.

- [25] K. Suresh, M. Takalloozadeh, Stress-constrained topology optimization: a topological level-set approach, *Structural and Multidisciplinary Optimization* 48 (2013) 295–309.
- [26] A. M. Mirzendehtdel, B. Rankouhi, K. Suresh, Strength-based topology optimization for anisotropic parts, *Additive Manufacturing* 19 (2018) 104–113.
- [27] N. Das, M. Yip, Learning-based proxy collision detection for robot motion planning applications, *IEEE Transactions on Robotics* 36 (4) (2020) 1096–1114.
- [28] C. Dai, S. Lefebvre, K.-M. Yu, J. M. Geraedts, C. C. Wang, Planning jerk-optimized trajectory with discrete time constraints for redundant robots, *IEEE Transactions on Automation Science and Engineering* 17 (4) (2020) 1711–1724.
- [29] J. Pan, X. Zhang, D. Manocha, Efficient penetration depth approximation using active learning, *ACM Transactions on Graphics (TOG)* 32 (6) (2013) 1–12.